Pieces of the puzzle

Helmi, A.; Navarro, J. F.; Nordstrom, B.; Holmberg, J.; Abadi, M. G.; Steinmetz, M.

Published in:
Monthly Notices of the Royal Astronomical Society

DOI:
10.1111/j.1365-2966.2005.09818.x

Publication date:
2006

Mon. Not. R. Astron. Soc. **365,** 1309–1323 (2006) doi:10.1111/j.1365-2966.2005.09818.x

Pieces of the puzzle: ancient substructure in the Galactic disc

Amina Helmi,[1⋆] J. F. Navarro,[2,3]† B. Nordström,[4,5] J. Holmberg,[6] M. G. Abadi[2]‡ and M. Steinmetz[7,8]§

[1]*Kapteyn Astronomical Institute, University of Groningen, PO Box 800, 9700 AV Groningen, the Netherlands*
[2]*Department of Physics and Astronomy, University of Victoria, Victoria, Canada BC V8P 1A1*
[3]*Max-Planck Institute for Astrophysics, Karl-Schwarzschild Strasse 1, D-85741 Garching, Germany*
[4]*Niels Bohr Institute, Juliane Maries Vej 30, DK-2100 Copenhagen, Denmark*
[5]*Lund Observatory, Box 43, SE-22100 Lund, Sweden*
[6]*Tuorla Observatory, University of Turku, Vaisäläntie 20, FIN-21500 Piikkiö, Finland*
[7]*Astrophysikalisches Institut Potsdam, An der Sternwarte 16, Potsdam 14482, Germany*
[8]*Steward Observatory, University of Arizona, Tucson, AZ 85721, USA*

Accepted 2005 November 1. Received 2005 November 1; in original form 2005 May 17

ABSTRACT

We search for signatures of past accretion events in the Milky Way in the recently published catalogue by Nordström et al., containing accurate spatial and kinematic information as well as metallicities for 13 240 nearby stars. To optimize our strategy, we use numerical simulations and characterize the properties of the debris from disrupted satellites. We find that stars with a common progenitor should show distinct correlations between their orbital parameters; in particular, between the apocentre (A) and pericentre (P), as well as their z-angular momentum (L_z). In the APL space, such stars are expected to cluster around regions of roughly constant eccentricity.

The APL space for the Nordström catalogue exhibits a wealth of substructure, much of which can be linked to dynamical perturbations induced by spiral arms and the Galactic bar. However, our analysis also reveals a statistically significant excess of stars on orbits of common (moderate) eccentricity, analogous to the pattern expected for merger debris. Besides being dynamically peculiar, the 274 stars in these substructures have very distinct metallicity and age distributions, providing further evidence of their extragalactic provenance. It is possible to identify three coherent groups among these stars, that, in all likelihood, correspond to the remains of disrupted satellites. The most metal-rich group ([Fe/H] > -0.45 dex) has 120 stars distributed into two stellar populations of $\sim$8 Gyr (33 per cent) and $\sim$12 Gyr (67 per cent) of age. The second group with $\langle$[Fe/H]$\rangle \sim -0.6$ dex has 86 stars and shows evidence of three populations of 8 Gyr (15 per cent), 12 Gyr (36 per cent) and 16 Gyr (49 per cent) of age. Finally, the third group has 68 stars, with typical metallicity around -0.8 dex and a single age of $\sim$14 Gyr. The identification of substantial amounts of debris in the Galactic disc whose origin can be traced back to more than one satellite galaxy, provides evidence of the hierarchical formation of the Milky Way.

Key words: Galaxy: disc – Galaxy: evolution – Galaxy: kinematics and dynamics – solar neighbourhood – Galaxies: evolution – Galaxies: formation.

1 INTRODUCTION

In the past two decades, our understanding of galaxy formation has made a giant leap forward, thanks to both theoretical and observational developments. We currently know the initial conditions from which all structures in the Universe formed. The recent *Wilkinson Microwave Anisotropy Probe* measurements of the power spectrum of density fluctuations imprinted on the cosmic microwave background are extremely well fit by a Lambda cold dark matter (ΛCDM)

⋆E-mail: ahelmi@astro.rug.nl
†CIARand Guggenheim Fellow.
‡CITA National Fellow, on leave from Observatorio Astronómico de Córdoba and CONICET, Argentina.
§David and Lucile Packard Fellow.

cosmogony (Spergel et al. 2003). Therefore, we are in a good position to study the formation and evolution of galactic systems within the ΛCDM concordance model (e.g. Mo, Mao & White 1998; Silk & Bouwens 2001). In this framework, galaxy formation proceeds hierarchically, from the collapse of small galactic subunits, which subsequently merge to produce large galaxies like our own (Benson et al. 2003; Springel & Hernquist 2003).

It has recently become possible to simulate the formation of a disc galaxy from first principles in a cosmological context (e.g. Bekki & Chiba 2001; Abadi et al. 2003a; Sommer-Larsen, Götz & Portinari 2003; Brook et al. 2004; Governato et al. 2004). Although the numerical resolution of these simulations (particularly the number of stellar particles) is far from ideal to study the detailed spatial and kinematic distribution of stars, they have provided us with useful insight into the formation process of a disc galaxy (see also Samland & Gerhard 2003). In particular, Abadi et al. (2003b) claim that a majority of the oldest stars in the disc, and the thick disc itself, originated in satellites accreted on low-inclination orbits. However, it is hard to establish whether this is a generic feature of hierarchical models because these conclusions were based on a single cosmological simulation.

In the context of the CDM framework, one would like to determine the merging history of the Milky Way. How many progenitor systems built up the Galaxy? What were their properties? What fraction of the stars located in a region like the solar neighbourhood formed in situ, what fraction originated in mergers? Have major mergers of gas-rich systems played an important role? Is the contribution of minor mergers significant? Although the hierarchical model may be fundamentally different from the collapse model proposed by Eggen, Lynden-Bell & Sandage (1962), they may have a few features in common. It is not unlikely that, early in the history of the Galaxy, there was a phase which could be described as a fast-dissipative collapse, but which was triggered by gas-rich mergers (Brook et al. 2004), rather than by the collapse of a giant cloud of gas. Nevertheless, it is also clear that collisionless minor mergers have also played a role in the formation of our Galaxy. This is evidenced by the presence of the disrupting Sgr dwarf (Ibata, Gilmore & Irwin 1994), the substructure in the Galactic halo (Helmi et al. 1999) and the (thick) disc (i.e. the Arcturus stream, Eggen 1996; Navarro, Helmi & Freeman 2004), the ring in the outer Galaxy (Yanny et al. 2003), the Canis Major dwarf (Martin et al. 2004; but see also Momany et al. 2004). This list of examples also serves to indicate that substructure appears to be ubiquitous, although the samples are still rather small to establish, even in a statistical sense, how important mergers have been in the history of the Galaxy.

The spatial and kinematic distribution of the debris from the accreted satellites is an aspect that has received more attention in the last few years (Johnston, Hernquist & Bolte 1996; Helmi & White 1999; Helmi, White & Springel 2003). For example, Helmi et al. (2003) using a combination of analytic work and cosmological simulations, concluded that there should be several hundred kinematically cold streams in the stellar halo near the Sun. This prediction is consistent with observations, while a full test would require an enlargement by a factor of 10 or so in the size of the samples of halo stars with accurate 3D kinematics. Nevertheless, Gould (2003) was able to infer statistically a limit on the granularity of the velocity distribution of halo stars, using a large sample of nearby dwarfs with proper motions. He confirmed that there are no streams with more than 5 per cent of the local density (consistent with the result of Helmi et al. 1999), and that there are at least 400 such streams present.

However, mergers and accretion are not the only source of substructure in a galactic disc. Conceivably, these could be the mechanisms that provide the least prominent contributions to the substructure observed in discs. Stars form generally in groups or clusters (Chereul, Crézé & Bienaymé 1998), spiral arms produce perturbations and resonances that confine stars temporarily to a small region of phase space (De Simone, Wu & Tremaine 2004), and the bar causes resonances which trap stars into structures such as the Hercules stream (Dehnen 1998, 2000; Fux 2001). Disentangling the various physical mechanisms responsible for the substructure observed is by no means trivial, and requires additional knowledge of the properties of the members of a given substructure. For example, the age and, in particular, the metallicity distributions of the Hercules stream are very broad, from −0.6 to +0.6 dex peaking around [Fe/H] ∼0 dex and with ages in the range 6–10 Gyr – and hence its origin cannot be attributed to an accreted satellite (Raboud et al. 1998). It is not inconceivable however, that streams with a merger origin do show a spread in ages and metallicity, particularly if the parent system was a relatively large satellite (see e.g. Navarro et al. 2004).

Interesting constraints on the process of galaxy formation can also be obtained from detailed analysis of the chemical abundances of stars (e.g. Cayrel et al. 2004). Recently, Venn et al. (2004) pointed out that the chemical composition (metallicity and abundance patterns) and age distribution of stars in the satellites of the Milky Way are significantly different from those found for stars in the halo and thin and thick discs of our Galaxy (see also Unavane, Wyse & Gilmore 1996). They concluded that these components cannot have accreted too many satellites like those currently orbiting the Milky Way. However, hierarchical models predict that any accreted population of stars is more likely to have originated in a few massive galaxies rather than in many dwarf galaxies. Furthermore, it remains to be seen if the progenitors of the present-day satellites could have, for example, built up the Galactic halo, if accreted at high redshift (as also suggested by Robertson et al. 2005). This hypothesis can be tested with accurate age determinations and abundance measurements of the oldest stellar populations in the dwarf galaxies and in the Galactic halo (Hill et al., in preparation).

In this paper, we analyse a recently published catalogue of stars in the solar neighbourhood (Nordström et al. 2004; hereafter N04), containing accurate full phase-space information and metallicities ([Fe/H]) for 13 240 stars. This sample is therefore ideal to look for substructures associated with past mergers. We begin our quest in Section 2 by describing the sample's properties. To guide our search for the signatures of disrupted galaxies, in Section 3 we characterize the properties of substructure induced by mergers, while we devote Section 4 to study the phase-space distribution of the stars in the N04 sample. In Sections 4.1–4.3 we establish the presence of substructures in the sample and study their properties in Sections 4.4 and 4.5. We summarize our results in Section 5.

2 OBSERVATIONAL SAMPLE

In this paper, we focus on the complete, all-sky, magnitude-limited, and kinematically unbiased sample of 14 139[1] F and G dwarf stars presented by N04. New accurate radial-velocity observations have been obtained by these authors which, together with published Strömgren $uvby\beta$ photometry, Hipparcos parallaxes, Tycho-2 proper motions and a few earlier radial velocities, complete the

[1] Full 6D phase-space information is available for 13 240 stars.

kinematic information. These high-quality velocity data are supplemented by effective temperatures and metallicities newly derived from recent and/or revised calibrations. Spectroscopic binaries have been identified thanks to multi-epoch radial velocity measurements.

F- and G-type dwarf stars are particularly useful to study Galactic evolution, being numerous and long lived; their atmospheres reflect their initial chemical composition; and their ages can be estimated for at least the more evolved stars by comparison with stellar evolution models. We will now summarize some important properties of the N04 sample and refer the reader to the original paper for a more comprehensive description.

Stars in the N04 sample were selected from a compilation of catalogues available in the literature with $uvby\beta$ photometry of nearby F and G stars, but mostly from the surveys by Olsen (1983, 1993, 1994a,b). The N04 sample is volume complete to roughly 40 pc. It is magnitude complete to $V \leqslant 7.7$ for the bluest stars (slightly fainter for the reddest G stars) and has a cut-off magnitude $V_{\rm cut} \sim 8.9$ (and 9.9 for the reddest G stars). The radial velocities are typically the result of two or more spectroscopic observations and have a typical mean error of 0.5 km s^{-1} or less. The proper motions for the vast majority of the stars are from the Tycho-2 catalogue (Høg et al. 2000), i.e. constructed by combining the Tycho star-mapper measurements of the Hipparcos satellite with the Astrographic Catalogue based on measurements in the Carte du Ciel and other ground-based catalogues. A small number of stars have only one measurement, either from Hipparcos or Tycho. The typical mean error in the total proper motion vector is 1.8 mas yr^{-1}.

Accurate trigonometric parallaxes are available from Hipparcos for the majority of the stars (ESA 1997), with relative errors (σ_π/π) generally better than 10 per cent. When the Hipparcos parallax is either unavailable or is less accurate than the photometric parallax, whose uncertainty is only 13 per cent, the latter is used. Photometric parallaxes are derived from the distance calibrations for F and G dwarfs by Crawford (1975) and Olsen (1984).

The accurate determination of metallicities for F and G stars is one of the strengths of the Strömgren $uvby\beta$ system. The calibrations used in the N04 paper were either already available (e.g. Schuster & Nissen 1989), or have been extended towards redder stars by comparison to spectroscopic metallicities from recently published high-resolution data. The typical uncertainty is of the order of 0.1 dex. This estimate relies, for example, on the excellent agreement with the Edvardsson et al. (1993) spectroscopic metallicities.

Individual ages are determined by means of a Bayesian estimation method that compares a grid of theoretical isochrones with the location of stars in the Hertzsprung–Russell (HR) diagram, using the observed $T_{\rm eff}$, M_V and [Fe/H], as well as their observational errors (Jørgensen & Lindegren 2005). In practice, isochrone ages can only be determined for stars that have evolved significantly away from the zero-age main-sequence (ZAMS). This precludes the determination of reliable isochrone ages for unevolved (i.e. relatively young) stars as well as for low-mass G and K dwarfs located on the ZAMS.

Fig. 1 shows the spatial distribution of the stars in the sample. Except for the concentration corresponding to the Hyades (at $x \sim -40$ pc, $y \sim 0$ pc, Perryman et al. 1998), the distribution of stars in space appears to be smooth.

In Fig. 2, we show the velocity distribution of the stars in the sample. The velocities are defined in a right-handed Galactic coordinate system with U pointing towards the Galactic centre, V in the direction of rotation and W towards the north Galactic pole. The Sun is located at $x = -8$ kpc and the velocities have been corrected for the solar motion using the values from Dehnen & Binney (1998) and

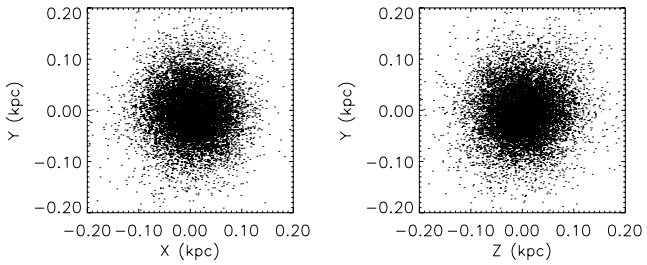

Figure 1. Spatial distribution of the stars in the Nordström et al. (2004) sample. Note that the sample is restricted to a small region around the Sun, being volume complete out to a distance of approximately 40 pc.

assuming a local standard of rest velocity of 220 km s^{-1}. It is evident from the top panels of Fig. 2 that most of the stars have a mean prograde motion, indicative of the dominant contribution of the Galactic thin disc to the current sample. There are few halo stars present, as evidenced by the small number of objects that cluster around zero rotational velocity and that have large radial and z-motions. The central panel of Fig. 2 focuses on the stars with disc-like kinematics. Large amounts of substructure are clearly present in the sample. The most prominent, and which can be easily picked up by eye, are the Hyades–Pleiades, Sirius and Hercules superclusters (Eggen 1958, 1960, 1975). Following the characterization by Famaey et al. (2005), we highlight these structures in the bottom panels of Fig. 2. There are 2103 stars associated with the Hyades–Pleiades structure, 1353 stars with the Sirius moving group, and 1071 stars with the Hercules stream in the N04 sample. These substructures are most likely associated to two phenomena unrelated to the merger history of the Galaxy. They are clusters of stars born in the Galactic thin disc (e.g. Hyades), or they are the result of perturbations by spiral arms or the Galactic bar which drive the dynamical evolution of the disc (e.g. Hercules stream).

Almost 99 per cent of the stars in the sample have accurate metallicities, which allows us to study how the mean velocity and the dispersion change with [Fe/H]. This is illustrated in Fig. 3 which shows the mean velocity components and velocity dispersions in the (U, V, W) directions as function of [Fe/H]. As extensively discussed in the literature (Sandage & Fouts 1987; Norris & Ryan 1989; Carney, Latham & Laird 1990; Nissen & Schuster 1991; Edvardsson et al. 1993; Chiba & Beers 2001) and, in particular, in the pioneering work of Eggen et al. (1962), there is a strong correlation between the kinematics and the metallicities of stars in the solar neighbourhood. In broad terms, the most metal-poor stars form part of a non-rotating, hot-component (halo), while the majority of the most metal-rich stars are in a fast-rotating, cold-component (disc).

3 INSIGHTS FROM NUMERICAL SIMULATIONS

3.1 The space of conserved quantities

The substructure associated with past accretion events is expected to have much lower density contrast than, for example, that associated with open clusters (e.g. Helmi & White 1999). This implies that sophisticated methods of identification need to be developed. For example, satellite galaxies of the size of the Small Magellanic Cloud are expected to contribute around 50 stellar streams to the halo in the solar neighbourhood. Such streams would have rather low density contrast, and therefore, identification of each one of them independently could be a rather daunting task. A better strategy is to

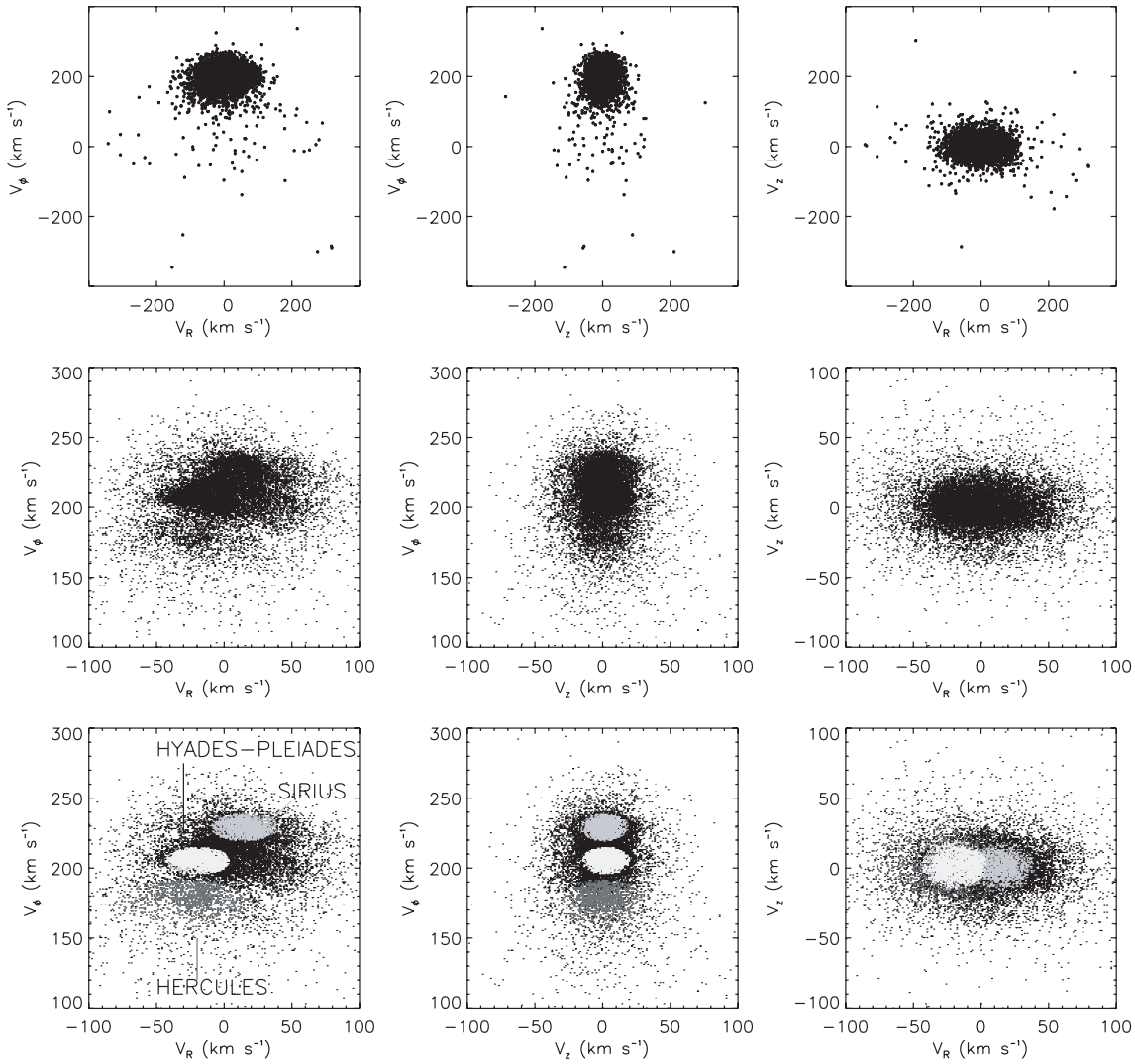

Figure 2. Top: Velocity distribution of stars in the N04 sample. The great majority of the stars have disc-like kinematics. Centre: Zoom-in of the top panels to show with higher resolution the velocity distribution of stars in the Galactic disc. It is immediately apparent that the kinematic distribution contains a large degree of substructure. Bottom: Identification of the Hyades–Pleiades, Sirius and Hercules superclusters in our sample according to the criteria of Famaey et al. (2005). These are the most prominent structures in velocity space.

identify a space in which all stars from such a satellite are clustered into a relatively small volume.

Helmi & de Zeeuw (2000) proposed that the space of energy, z-component of the angular momentum and total angular momentum (E, L_z, L) would be well suited for identifying debris from disrupted satellites. They based this conclusion on simulations of the disruption of roughly thirty small satellites with orbits in the inner halo, i.e. with debris contributing to the solar neighbourhood. They found that the particles from the satellites remained strongly clumped, even after 10 Gyr of evolution, in the space of energy, L_z and total angular momentum. Their simulations were rather simplistic, since the satellites were evolved in a fixed potential, but highlighted that recovery would be possible in a space of quasi-conserved quantities. In a hierarchical Universe, the total energy of a satellite is not a conserved quantity, since strong fluctuations in the gravitational potential are expected to have been important throughout the build-up of galactic systems. Massive satellites also suffer from dynamical friction, implying that the stars lost in different passages end up having different energy levels, an effect which is visible for example, in the work of Knebe et al. (2005). Moreover, the total angular momentum is not a conserved quantity either, even in the static case considered by Helmi & de Zeeuw (2000), because the Galactic potential is not spherical. Hence, it is clear that a new approach is required beyond that previously proposed.

3.2 The APL space

Let us first explore the characteristics of debris from a disrupted satellite in the 'fixed-potential' regime. We focus here on a simulation that reproduces the properties of the Arcturus group and that was presented in Navarro et al. (2004). In this simulation, we represent the satellite by 10^5 particles that follow a King sphere with concentration $c = \log_{10} r_t/r_c = 1.25$ and core radius 0.39 kpc. Its initial 1D velocity dispersion is 18.6 km s^{-1}, while its total mass is $M_{\rm sat} = 3.75 \times 10^8\,{\rm M}_\odot$.[2] This simulation models the self-gravity of

[2] These numerical values differ from those quoted in Navarro et al. (2004) due to a typographical error.

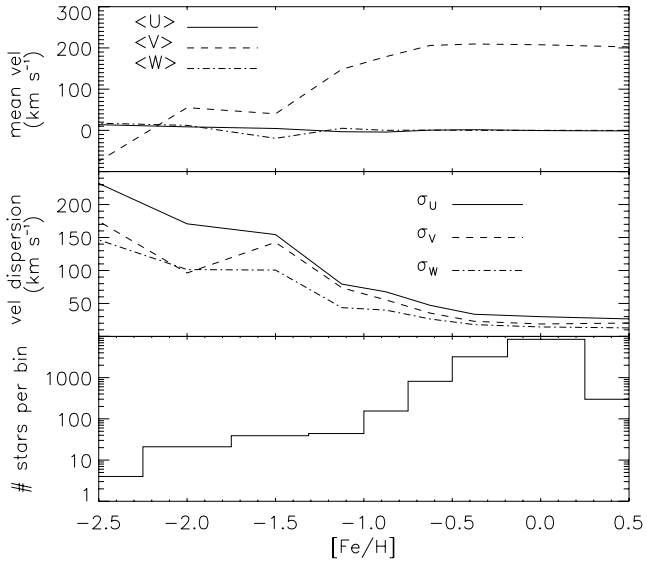

Figure 3. Mean velocity components and dispersion as function of metallicity [Fe/H] for the stars in the N04 sample. The bottom panel shows that there are only a handful of objects in the most metal-poor bins, which makes less reliable the characterization of the velocity ellipsoid.

the satellite using a quadrupole expansion of the internal potential (Zaritsky & White 1988), but is otherwise run in the fixed Galactic potential $\Phi = \Phi_{\rm halo} + \Phi_{\rm disc} + \Phi_{\rm bulge}$, where

$$\Phi_{\rm halo} = v_{\rm halo}^2 \ln\left(1 + \frac{R^2}{d^2} + \frac{z^2}{d^2}\right), \tag{1}$$

with $v_{\rm halo} = 134\,{\rm km\,s^{-1}}$ and $d = 12\,{\rm kpc}$,

$$\Phi_{\rm disc} = -\frac{GM_{\rm disc}}{\sqrt{R^2 + \left(a_{\rm d} + \sqrt{z^2 + b_{\rm d}^2}\right)^2}}, \tag{2}$$

with $M_{\rm disc} = 9.3 \times 10^{10}\,{\rm M}_\odot$, $a_{\rm d} = 6.5\,{\rm kpc}$ and $b_{\rm d} = 0.26\,{\rm kpc}$, and

$$\Phi_{\rm bulge} = -\frac{GM_{\rm bulge}}{r + c_{\rm b}}, \tag{3}$$

with $M_{\rm bulge} = 3.4 \times 10^{10}\,{\rm M}_\odot$ and $c_{\rm b} = 0.7\,{\rm kpc}$. The numerical values of the relevant parameters in these models are chosen to provide a good fit to the rotation curve of the Milky Way. The satellite's orbit has apocentre ∼9.3 kpc, pericentre ∼3.1 kpc, eccentricity $\epsilon = (r_{\rm apo} - r_{\rm peri})/(r_{\rm apo} + r_{\rm peri}) \sim 0.5$ and $L_z \sim 970\,{\rm kpc\,km\,s^{-1}}$.

In Fig. 4 we show the velocities of the particles from the satellite after 8 Gyr of evolution. We focus on a sphere centred on the 'Sun' (at 8 kpc from the galaxy's centre) of 1.5 kpc radius. The 'banana' shape seen in the first panel of this figure, defined by the V_ϕ and V_R velocities, is due to the presence of groups of particles

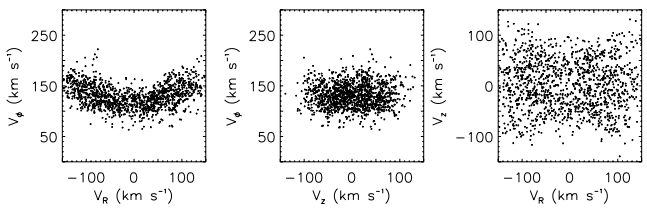

Figure 4. Velocity distribution of particles from a simulated satellite, 8 Gyr after infall. The particles are located in a sphere centred on the 'Sun' of 1.5 kpc radius.

with slightly different orbital phases. Particles located at apocentre now have $V_R \sim 0\,{\rm km\,s^{-1}}$, while those moving towards or away from their apocentres, have positive or negative V_R, respectively. As we shall see later, this very characteristic banana shape is present whenever a group of stars have similar orbital eccentricities. Note as well from Fig. 4 the symmetry in V_R and V_z, which reflects the high degree of mixing of the particles. The velocity distribution of satellite debris is notably different from that associated to substructures produced by dynamical resonances (see bottom panel of Fig. 2). Its characteristic shape will later enable us to make a distinction between substructures associated to satellite debris and those due to dynamical processes.

Instead of the energy–L_z–angular momentum space, we now focus on that defined by orbital apocentre–pericentre–L_z, i.e. the APL space. After some experimentation, we found that this space appears to be very suitable for our goals of finding accretion relicts. Fig. 5 shows the distribution in the APL space of the particles in our simulation, after 8 Gyr of evolution. The black solid points correspond to particles located inside a sphere of 1.5 kpc radius centred on the 'Sun' (the same volume as that used in Fig. 4), while the grey dots are within a larger sphere of 5 kpc radius. The particles are not scattered throughout the APL space but occupy a relatively small region. The extent of this region is determined by the initial size of the system (since dynamical friction or other dynamical processes that could affect the extent are not included in the simulation). In the pericentre versus apocentre projections the particles distribute themselves around a curve of constant eccentricity (shown as the solid line).

There is little difference between the distribution of black and grey points in Fig. 5, which indicates that even particles within a small volume sample the whole extent of the satellite in the APL space. This is because enough time has passed since infall for these particles to phase-mix and be distributed in a number of different streams that are crossing the particular volume under consideration. In this case, there are around 10 different streams, which can be identified as the streaks in the different projections of the APL space. Particles on the same stream have similar apocentres, pericentres and L_z, but these quantities are correlated and hence not completely independent from one another. These correlations are then reflected in the streaks (or curves/surfaces connecting the variables) which are visible in the various projections of the APL space. In other words, the topology of a stream in phase space could, in principle, be even better characterized using a different set of (orthogonal) variables that are some combination of apocentre, pericentre and L_z.

When a satellite galaxy is accreted in a time-dependent gravitational potential or when it suffers dynamical friction, the distribution of its particles in the APL space will be slightly different. As in the static case, stars lost in the same passage are expected to have more

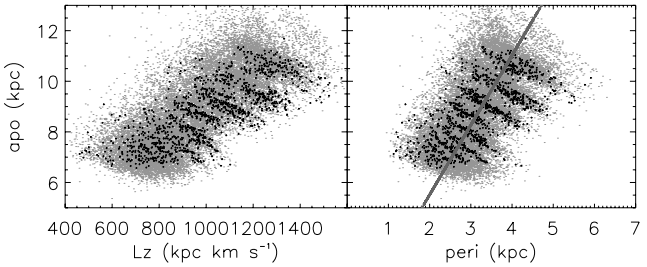

Figure 5. Distribution of particles in the APL space for the simulation shown in Fig. 4. The black (grey) points represent particles located in a solar neighbourhood volume of 1.5 kpc (5 kpc) radius centred on the Sun.

similar orbital parameters (including pericentric and apocentric distances) than those lost in other passages.[3] Changes in the Galactic potential are likely to occur on time-scales longer than one orbital period of the satellite, implying that those stars lost in the same passage will remain clumped together and presumably perturbed on to a different orbital path (with larger binding energy if the galaxy has, for example, gained a large amount of mass in the inner regions during a major merger). A similar argument holds if dynamical friction is important. Massive satellites will deposit stars in different energy levels, according to the time/passage when the stars were released. So, to first order, one expects stars to generally cluster in the APL space and along a line of constant eccentricity also in a time-dependent situation.

3.3 Galaxy formation simulations

It is important to confirm our conclusions about the evolution of debris in time-independent gravitational potentials. We need to establish whether the APL space is a conserved-quantities space also under the conditions found in a hierarchical universe.

Hence, it is necessary to turn to simulations of the formation of galaxy discs which take into consideration all possible dynamical effects, including the evolution of the Galactic potential and dynamical friction, collisions between satellites, etc. Abadi et al. (2003a) present one such high-resolution simulation that models the formation of a disc galaxy, albeit of an earlier type than the Milky Way. Nevertheless, we expect that the gross characteristics of the dynamical evolution of substructure will not depend strongly on the exact properties of the main galaxy (provided the simulation represents a disc and not, e.g. a highly triaxial system). An important ingredient of this simulation is the self-consistent modelling of star formation, which allows the distinction between star particles and dark-matter particles. This is advantageous for our purposes since we expect the identification of stellar substructures to be easier than that of their dark-matter counterparts. This is because the dark matter occupies a larger region of phase space than the stellar components of galaxies (which are typically more concentrated to the centres of the halos in which they are embedded). Hence, stellar substructures should have a higher density contrast and be less convoluted (spatially) than the dark matter. All these imply that the chance of superposition of lumps in the APL space ought to be smaller for stars than for dark matter.

We have selected 10 satellites in the simulation by Abadi et al. (2003a), with masses in the range 6×10^9–$2.7 \times 10^{10}\,\mathrm{M}_\odot$, which merge with the central galaxy in the redshift range 3.4–1. Figs 6 and 7 show the evolution of one of these satellites. Its total mass at the time of infall (at redshift $z = 1.05$) was $1.1 \times 10^{10}\,\mathrm{M}_\odot$, while its stellar mass (represented by ∼5000 particles) was $4.5 \times 10^9\,\mathrm{M}_\odot$. Efficient dynamical friction brings it to the inner galaxy, and so this satellite contributes star-particles to the solar circle. A fair fraction of this debris is deposited on eccentric orbits in the galactic disc (Abadi et al. 2003b).

In Fig. 8, we show the present-day velocities of the star-particles originating in those 10 satellites, for a 4-kpc box centred on the solar circle. We have highlighted the contribution of the satellite shown in Figs 6 and 7. There are some hints of moving groups (around $V_\phi \sim 80\,\mathrm{km\,s^{-1}}$, $V_\phi \sim 120\,\mathrm{km\,s^{-1}}$ and $V_\phi \sim 200\,\mathrm{km\,s^{-1}}$), but clearly the number of particles is too small to fully resolve the velocity distribution into substructures.

We now proceed to determine the distribution in the APL space for the star-particles in our simulation. We compute the apocentric and pericentric distances through orbital integration in the Galactic potential introduced in Section 3.2. Note that this potential does not constitute a very good model of our simulated galaxy, which is of earlier-type (Sa) than our Galaxy. However, this is done

[3] In reality, at each pericentric passage two groups of stars are released, defining a trailing and a leading stream. The properties of the stars in each of these streams are expected to be similar, while the energies of the trailing and leading streams should be offset (Johnston 1998; Mayer et al. 2002).

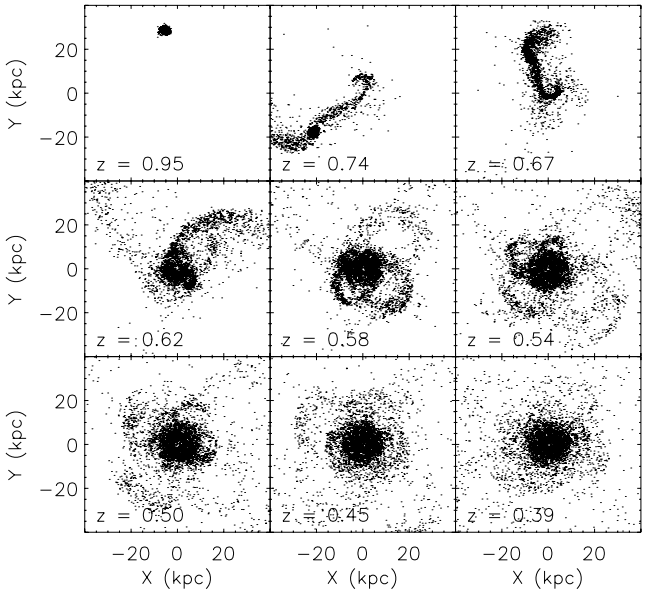

Figure 6. Face on view of the spatial distribution of the star-particles from a satellite identified in a high-resolution cosmological simulation. The satellite starts to merge with the host galaxy at $z = 1$, and after a few orbits it is completely disrupted.

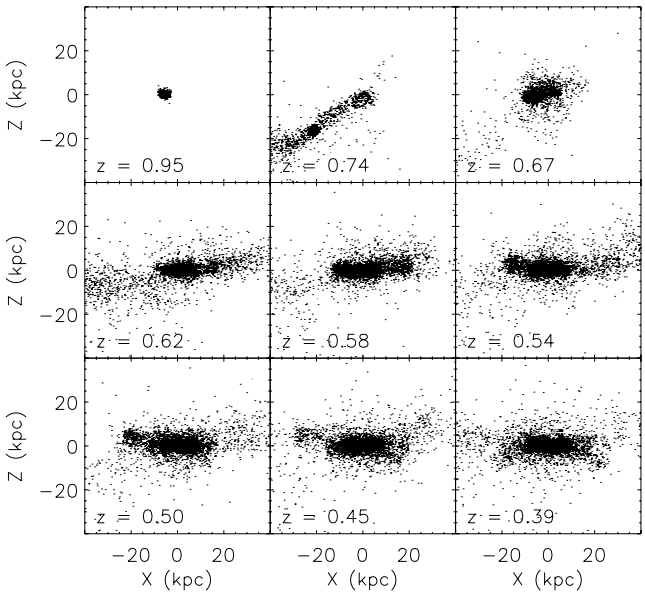

Figure 7. The same satellite as Fig. 6 but now the distribution of star-particles is shown in an edge-on view. Most of the debris of the satellite is deposited in a thick disc-like configuration.

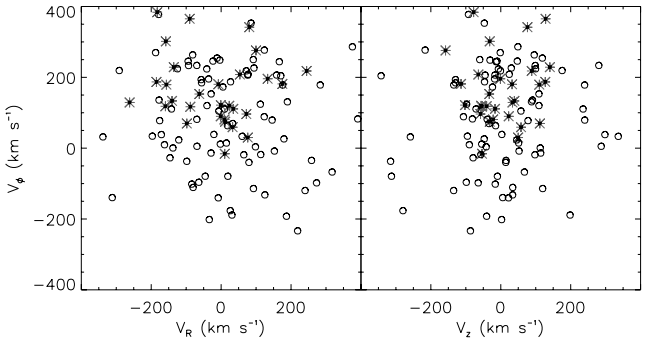

Figure 8. Velocity distribution of star-particles located in a box centred on the equivalent of the solar vicinity. We show the particles originating in 10 satellites identified in the cosmological simulation (open circles), and highlight (asterisks) the contribution of the satellite shown in Figs 6 and 7.

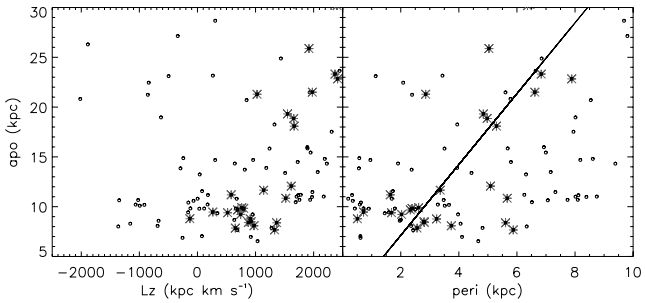

Figure 9. APL space distribution of star-particles located in a box centred on the solar circle. We show the particles originating in ten satellites identified in the cosmological simulation (open circles), and highlight (asterisks) the contribution of the satellite shown in Figs 6–8. Notice that the distribution is much lumpier than the velocity distribution shown in Fig. 8. The horizontal streaks visible in the apo–peri plot, particularly for the asterisks, correspond to groups of star-particles which have, presumably, become unbound around the same time. Note as well the diagonal pattern defined by the asterisks in both projections of the APL space. This pattern is the same as that shown in Fig. 5 for the satellite evolving in a static Galactic potential. The pattern shows that the debris is distributed along a line of (quasi)-constant eccentricity as indicated by the solid line in the right-hand panel.

intentionally since observers will only approximately know the form of the underlying potential.

In Fig. 9, we show the APL space distribution of star-particles located in the same 4-kpc box we showed before. The asterisks in this figure correspond to the star-particles originating in the satellite shown in Figs 6–8. The distribution is clearly lumpy, in stark contrast to the velocity distribution shown in Fig. 8, providing support for our hypothesis that the APL is a space of quasi-conserved quantities. Note that this satellite has produced several lumps in the APL space: the 'horizontal stripes' in the peri–apo presumably correspond to star-particles released in a given perigalactic passage. Such features are common to all satellites, as evidenced by the distribution of open circles in Fig. 9 and which corresponds to the 10 satellites identified in the simulations that contribute to this volume.

4 ANALYSIS OF THE N04 SAMPLE

4.1 Distribution of the data in the APL space

The analysis performed on the galaxy formation simulations gives us confidence that even in the fully hierarchical regime, the substructure

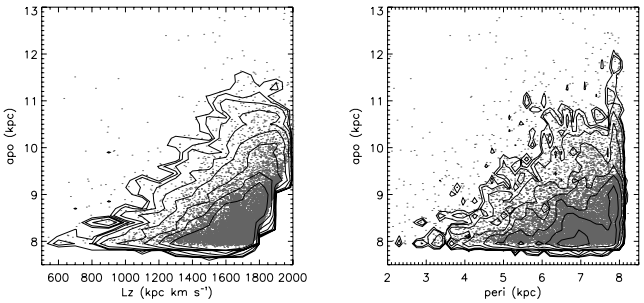

Figure 10. Distribution of the stars in the N04 sample in the APL space. The contours help visualize the very lumpy nature of the sample.

associated to past mergers remains relatively intact in phase space. The signatures from (or left by) accreted satellites remain coherent in the APL space.

Fig. 10 shows the distribution in the APL space of the stars in the N04 sample. The largest uncertainties in the location of a star in this space are not due to observational errors (which are typically less than 1.5 km s^{-1} in the velocity), but in the limited knowledge of the form of the Galactic potential used to determine the orbital parameters (apocentre and pericentre). However, we do not expect this uncertainty to strongly affect the distribution of points in the APL space. The volume probed by the N04 sample is so small that the Galactic potential is close to constant inside this region. This implies that the energy, and hence the orbital parameters or the location of a star in the APL space, are determined mostly by its kinematics, rather than by its spatial location (or the Galactic potential). Changes in the Galactic potential produce only small variations in the orbital parameters. For example, in the case of the potential proposed by Flynn, Sommer-Larsen & Christensen (1996), we find a typical change of 1–2 per cent in apocentre and pericentre.

Small moving groups, such as the Hyades open cluster, define very tight structures in phase space, and this is also reflected in their characteristic sizes in the APL space. For example, the stars in the Hyades open cluster have apocentre ∼8.52 kpc, pericentre ∼6.85 kpc and $L_z \sim 1659$ kpc km s^{-1}, while the dispersions around these mean values are $\sigma_{\rm apo} \sim 0.05$ kpc, $\sigma_{\rm peri} \sim 0.07$ kpc and $\sigma_{L_z} \sim 11$ kpc km s^{-1}. On the contrary, substructures due to past mergers will generally be more extended in APL space, as evidenced in Figs 5 and 9, where typically $\Delta_{\rm apo,\,peri} \sim 0.5$–1 kpc and $\Delta L_z \sim 200$–400 kpc km s^{-1}.

It is clear from Fig. 10 that the distribution of stars in the APL space is rather lumpy, as shown by the iso-density contours. A large fraction of the substructures are not only found in the 'tails' of the distribution of data points, but also right where the density of points is highest. The most prominent of these structures are actually due to the Hyades–Pleiades, Sirius and Hercules superclusters that were identified in Fig. 2. These occupy a region of the APL space dominated by disc-like and low-eccentricity orbits, with $\epsilon \leqslant 0.2$.

There are two issues that need to be addressed before accepting the hypothesis that the substructures observed in Fig. 10, and which are not associated to open clusters or superclusters, are due to past mergers. The first issue is to establish how many of those substructures are simply statistical fluctuations of otherwise smooth distributions. This is addressed in Sections 4.2 and 4.3 through Monte Carlo simulations. A second issue concerns the interpretation of these structures as satellite debris. We will address this in Sections 4.4 and 4.5, where we look in detail into the properties of the different structures discovered.

4.2 Monte Carlo simulations of a smooth galaxy

It is extremely important to understand the expected characteristics of a smooth galaxy for a data set like the N04 sample. This is crucial for a proper statistical assessment of the substructure observed in Fig. 10. To produce a smooth model of the Milky Way, one may proceed by generating individual structural components: thin and thick disc, halo and bulge components each with their characteristic spatial, kinematic and metallicity distribution (Robin et al. 2003). However, we prefer to follow a simpler approach that consists of combining the observed spatial distribution of the stars in the sample, with random velocities that reproduce the behaviour of the velocity ellipsoid with metallicity shown in Fig. 3.

As previously discussed, the spatial distribution of the stars in the sample is relatively smooth, and hence we can use it directly as input for our Monte Carlo models of the Galaxy. On the contrary, the observed kinematic distribution is rather lumpy (as shown in Fig. 2). Therefore, we only need to replace this distribution by a multivariate Gaussian to obtain a smooth model of the Galaxy. It is worth noting that we do not expect any correlations between the spatial and kinematic distribution of the stars, because the volume probed by these observations is sufficiently small that the various Galactic components cannot be distinguished solely on the basis of the spatial distribution of the stars in the sample.

The velocity distribution in our Monte Carlo simulations is represented by a set of multivariate Gaussians whose characteristic parameters are allowed to vary with metallicity in the manner given by the data itself (see Fig. 3). The orientation of the principal axes of the velocity ellipsoid do not perfectly coincide with the U, V, W directions and vary slightly in each metallicity bin. Our 1000 Monte Carlo simulations have the same number of stars in each metallicity bin as the original data, as well as the same spatial distribution. Thus each 'Monte Carlo star' is given a random velocity as described above and assigned spatial coordinates from the original data set.

4.3 Statistical analysis of the sample

We are now ready to compare the distribution of the observed data points and the smooth Galaxy model in the APL space. We compute the orbital properties in the Galactic potential characterized by equations (1)–(3), for each of the 13 092 points in our 1000 Monte Carlo samples.[4] Fig. 11 shows an example of the distribution of points in the case of the smooth Galaxy model. The overall characteristics (extent, high concentration of points on disc-like orbits) of the distribution are in good agreement with the observations (see Fig. 10), and support the assumptions made to generate a smooth model of the Galaxy. Eye-ball inspection shows that the distribution is not completely featureless (particularly in the apocentre versus pericentre projection). A direct comparison to Fig. 10 suggests, however, that the N04 sample contains far more substructure (also in the regions that would be dominated by the young-disc stars, i.e. pericentre ∼6–8 kpc and apocentre ∼8 kpc).

We now wish to establish which regions of this 3D space show a statistically significant excess of stars compared to a smooth Galaxy. For this quantitative analysis, we make a partition of the APL space into cells, in which we perform number counts. We test three different partitions in each dimension: (45, 135, 225) × (19, 52, 85) × (6, 18, 30) in the apocentre, pericentre and L_z-directions, respectively. These correspond to a resolution (cell size) of (0.5, 0.17, 0.1) (kpc) × (0.45, 0.16, 0.1) (kpc) × (500, 166.7, 100) (kpc km s^{-1}), respectively. These cell sizes are comparable in extent to the substructures visible in the N-body simulations shown in Figs 5 and 9; they are typically much larger than expected for open clusters although comparable to the extent of the superclusters, as discussed in Section 4.1. For each cell j we compute the observed number of stars $N_j^{\rm obs}$ and the average number of points from the Monte Carlo realizations $\langle N_j \rangle$ and the dispersion around this average, σ_j. To establish which cells have a statistically significant excess of stars, we define s_j and p_j as

$$s_j = \frac{N_j^{\rm obs} - \langle N_j \rangle}{\sqrt{N_j^{\rm obs} + \sigma_j^2}} \tag{4}$$

which measures the excess of stars in each cell, weighted by the average expected 'dispersion' in the cell, and

$$p_j = \frac{{\rm e}^{-\lambda_j} \lambda_j^{x_j}}{\Gamma(1 + x_j)} \tag{5}$$

where $\lambda_j = \langle N_j \rangle$ and $x_j = N_j^{\rm obs}$. Therefore p_j measures the probability of observing x_j stars in cell j if the counts follow a Poisson distribution, whose characteristics are determined by the distribution of points from the Monte Carlo simulations. When the number of stars in a given cell is large, one may assume that the Gaussian limit has been reached and then s_j is the right statistic to use. In that case, we consider cells for which $s_j \geqslant 3$ to show a statistically significant overdensity. However, when the number of stars in a cell is not very large (typically less than 20), it is best to use the second statistic, and to identify significantly overdense cells as those for which $p_j \leqslant 0.01$ and $s_j > 0$.

In Fig. 12, we have plotted the location of the cells that show a significant overdensity according to the above criteria. Because of the 3D nature of the APL, we show slices of the apocentre versus pericentre space. This figure corresponds to a partition of 45 × 19 × 18 cells, or equivalently, to cell sizes of 0.5 × 0.45 × 166.7 kpc km s^{-1}. The colour coding indicates how statistically significant the overdensity is: from $10^{-3} \leqslant p < 10^{-2}$ (light grey) to $p < 10^{-5}$ (black). The regions identified also appear as significant overdensities for other choices of the partition. We are therefore confident that these results do not depend strongly on the cell size.

The cells that show the most significant overdensities are located in a region of the APL space which is largely dominated by thin disc stars (bottom central and right-hand panels), and which in fact coincides with the location of the superclusters as defined by Famaey

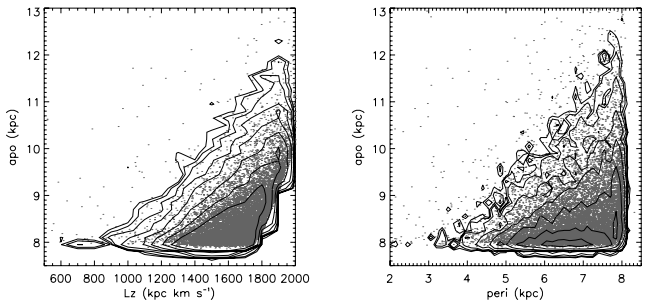

Figure 11. Distribution of points from one of our Monte Carlo simulations of a smooth Galaxy. The contours help to visualize the degree of lumpiness of the distribution in this space. The distribution of points with disc-like kinematics is much smoother than that of the N04 sample shown in Fig. 10. The contour levels are the same as in Fig. 10.

[4] The number of stars used to define the Monte Carlo simulations differs from the number of stars with full phase-space information in the N04 sample (13 092 instead of 13 240), because there are 148 stars that do not have a metallicity estimate.

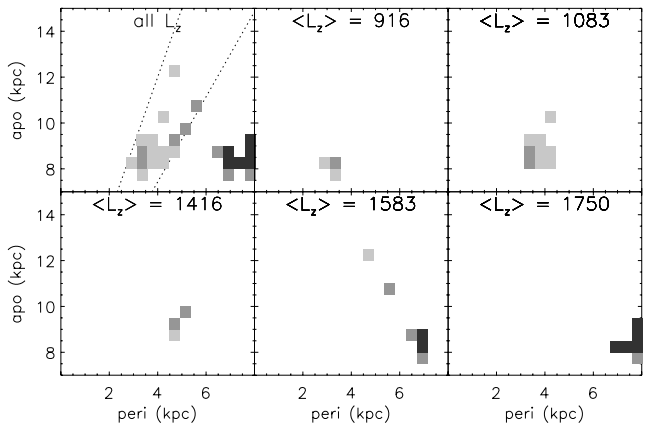

Figure 12. Distribution of overdense cells in the APL space. In the first panel we show a projection of the cells on to apocentre–pericentre space, while the rest of the panels correspond to slices in L_z, i.e. a narrow range of L_z values, and hence help visualize the 3D nature of the APL space. The colour coding indicates the statistical significance in steps of 10: black corresponds to $p < 10^{-5}$, dark grey to $10^{-5} \leqslant p < 10^{-4}$, grey to $10^{-4} \leqslant p < 10^{-3}$ and light grey to $10^{-3} \leqslant p < 10^{-2}$. Notice the diagonal patterns of overdensities that extend from apocentre ∼8–9 kpc, pericentre 3.5–4 kpc and which also have increasing L_z. They are very reminiscent of the structures produced by disrupted satellites and shown in Figs 5 and 9. The overdense cells are located in a segment of the APL space delimited by eccentricity $\epsilon \sim 0.3$–0.5, as indicated by the dotted lines in the first panel.

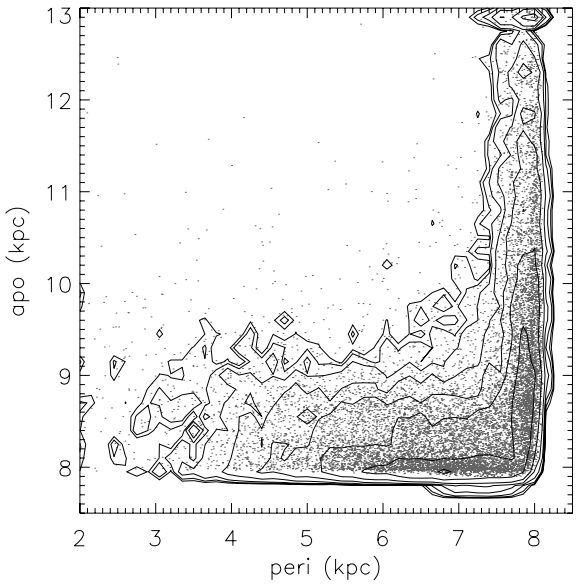

Figure 13. Distribution of points in the apocentre–pericentre projection of the APL space for one realization of the Besancon model of the Galaxy. By comparing to the panel on the right in Fig. 10 we note that this distribution is significantly different than that found for the N04 sample.

et al. (2005). The presence of overdensities in this region is likely the result of dynamical perturbations induced by asymmetries in the Galactic potential, such as the spiral arms and the Galactic bar, as shown by Dehnen (1998) and De Simone et al. (2004). Clearly, a Gaussian distribution does not provide a good representation of the kinematics of thin disc stars (of young to intermediate age), and it will be interesting to try and reproduce the features observed here with very detailed dynamical modelling and specify from more general principles the distribution function and its evolution in phase space (see Quillen & Minchev 2005, for a recent attempt).

Another intriguing feature of Fig. 12 are the overdensities located on a diagonal pattern in the apocentre versus pericentre projection, and which have progressively larger L_z. This pattern is very reminiscent of that produced by satellite debris, as shown in Figs 5 and 9. It is therefore natural to believe that these substructures are indeed the remains of disrupted satellites.

As discussed in Sections 3.2 and 3.3, such overdensities fall close to a line of constant eccentricity, which is reflected in the diagonal pattern observed in the projections of the APL space. In the observations, the overdense cells are limited by eccentricities $\epsilon_{\rm min} \sim 0.3$ and $\epsilon_{\rm max} \sim 0.5$ (the dotted lines in the first panel of Fig. 12).

One may question whether these overdensities are real, or simply the result of a poor choice of the comparison (smooth) model of the Galaxy. In an attempt to understand this, we turn to the Besancon model of the Galaxy. This is a standard model of the Galaxy, with thin and thick disc, as well as bulge and halo components (Robin et al. 2003, 2004). We have used the machinery provided on the Besancon website (http://bison.obs-besancon.fr/modele/) to generate samples of 'stars' with the same magnitude and colour limits as the N04 sample. We then calculate their orbital parameters in the Galactic potential given by equations (1)–(3), and determine their distribution in the APL space. Through this exercise, we find that the Besancon Galaxy model has an even smaller number of 'stars' in the region occupied by the overdensities, as shown in Fig. 13. Therefore, even for two rather different ways of making smooth Galaxy models, we obtain significant overdensities along a constant eccentricity segment in the APL space. This suggests that our interpretation of the data is statistically robust and may be the only viable one.

4.4 Focus on the overdensities

4.4.1 Metallicity distribution

We now proceed to study in more detail the properties of the stars located in this segment of eccentricities. The left-hand panel of Fig. 14 shows the metallicity distribution of these stars (black histogram). For comparison, we also plot the distribution of a control set of rather similar kinematics ($0.28 < \epsilon < 0.3$, dotted histogram) and the metallicities of the full sample (grey solid histogram). Note that the metallicity distribution of the full sample is rather narrowly concentrated around a peak value of [Fe/H] ~ -0.2 dex, which is close to the mean metallicity of the thin disc in this sample, i.e. $\langle$[Fe/H]$\rangle_{\rm disc} \sim -0.13$ dex (derived from stars with $|V_z| \leqslant 30\,{\rm km\,s^{-1}}$ and $\epsilon \leqslant 0.1$). The metallicity distribution of stars in the selected segment of eccentricities $\epsilon \in [0.3, 0.5)$ is much flatter and broader, and therefore significantly different. In fact, the probability that the selected set has been randomly drawn from the full sample, as measured by a KS test (Press et al. 1988) is less than 10^{-8}.

The metallicity distribution of the control set is also strikingly different from that of the selected set, despite their small difference in orbital eccentricities. It resembles more closely the distribution of the full sample, although it has a more pronounced tail towards lower metallicities. The KS test applied to the control and selected sets gives a probability that the two have the same parent metallicity distribution of approximately 10^{-4}, while the probability for the control and the full samples is 3 per cent. Clearly, there is a sharp transition in the properties of stars above and below $\epsilon \sim 0.3$, not just in terms of the degree of dynamical substructure but also in their metallicity distribution. The stars located in the region defined

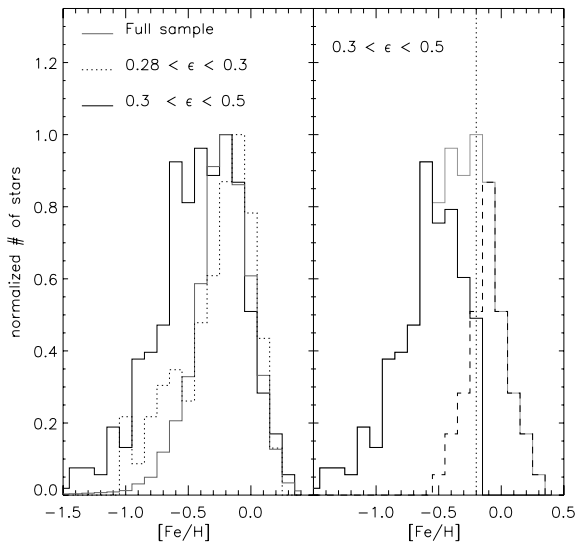

Figure 14. Left-hand panel: [Fe/H] distribution for the full N04 sample (grey), for the stars located in the segment of eccentricity defined by the overdense cells in Fig. 12 (black) and for a comparison set (dotted). Note the distinctly different metallicity distribution of the stars located in the overdensities in comparison to the full sample, and in particular to the set that has just slightly different orbital characteristics. Right-hand panel: The solid black histogram shows the metallicity distribution of the stars located in the segment $\epsilon \in [0.3, 0.5)$, after subtracting the contribution of the thin disc (dashed). The vertical dotted line corresponding to [Fe/H] $= -0.2$ dex, serves to indicate that to its left-hand side, the contamination by thin disc stars is small.

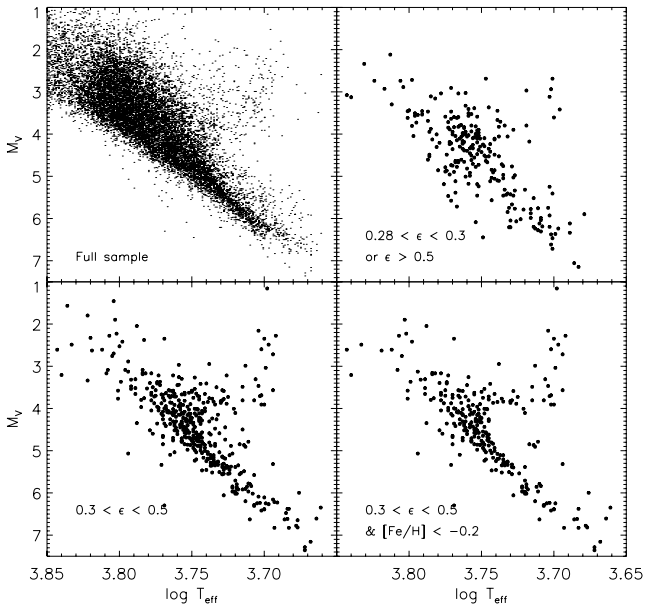

Figure 15. HR diagram of the full N04 sample (top left-hand panel); of a comparison set with lower/higher eccentricities than the overdense segment (top right-hand panel); of the set of stars located in the overdense segment (bottom left-hand panel); and a subset of the latter with lower metallicity (bottom right-hand panel). The bottom panels show the well-populated red giant branch and the dearth of luminous stars above $M_V \sim 3.8$, which suggests the presence of a turn-off point around that luminosity. Furthermore, notice how different the HR diagrams on the top and bottom rows are.

by the overdense cells with $0.3 \leqslant \epsilon < 0.5$ appear to constitute a separate class.

Even in this relatively high eccentricity range, contamination by thin disc stars is likely to be important. In the right-hand panel of Fig. 14, we plot again the metallicity distribution of stars in the selected segment of eccentricities (grey histogram). It is safe to infer that in this set, all stars with [Fe/H] $> \langle$[Fe/H]$\rangle_{\rm disc}$ belong to the thin disc. By assuming that the stars are symmetrically distributed with respect to $\langle$[Fe/H]$\rangle_{\rm disc}$, we can actually subtract their contribution (dashed histogram). Therefore, we obtain a 'cleaner' metallicity distribution of the stars in the selected segment of eccentricities (shown as the solid black histogram). This distribution shows a prominent peak at [Fe/H] ~ -0.6 and a broad 'bump' around [Fe/H] ~ -0.8. For the sake of simplicity, in what follows we will restrict further analysis to stars in the selected segment of eccentricities with [Fe/H] < -0.2 dex (i.e. to the left-hand side of the vertical dotted line in Fig. 14).

4.4.2 HR diagrams

Further insight into the properties of the stars located in the overdense segment of eccentricities can be obtained from the HR diagram. Effective temperatures have been determined from the Strömgren colours using the indices and calibrations of Alonso, Arribas & Martínez-Roger (1996), while the absolute magnitudes are known thanks to the distance information available for the stars in the sample.

The top left-hand panel of Fig. 15 shows the HR diagram of the stars in the N04 sample, while that on the top right-hand panel corresponds to a comparison set with eccentricities which are slightly different from those found in the overdense cells. The panel on the lower left-hand side shows the HR diagram for all stars in the overdense segment of eccentricities, i.e. with $0.3 \leqslant \epsilon < 0.5$, while that on the right-hand side corresponds to the subset of these stars that have [Fe/H] < -0.2 dex (minimizing the contamination by the thin disc). The two-most striking features in the lower HR diagrams are the presence of a well-defined red giant branch (perhaps more than one), and a possible corresponding turn-off around $M_V \sim 3.8$, which is visible thanks to the apparent dearth of stars with higher luminosities (younger ages). The elimination of stars with high metallicity further enhances the coherent features in the HR diagram of the overdense eccentricity segment, and provides more confidence that we have identified the debris of one or more disrupted galaxies. The stars in the overdense regions have a strikingly different age distribution than their parent sample (and than the control set shown in the top right-hand panel).

4.5 Characteristics of the satellites

4.5.1 How many?

One of the most interesting questions in the context of the formation of the Galaxy in a hierarchical Universe is, how many progenitors had it had and what were their characteristics? Therefore, it is very important to gauge the number of satellites that have given rise to the structures with eccentricity $0.3 \leqslant \epsilon < 0.5$. It is clear from the metallicity distribution shown in Fig. 14 that the satellites that have contributed to this region of phase space, must have been relatively massive to be able to contribute a large number of stars with [Fe/H] ~ -0.5 dex. The extent of the overdensities in the APL space are similar to that seen in the simulation discussed in Section 3.2, which corresponds to a satellite of $\sim 4 \times 10^8\,{\rm M}_\odot$ in stars.

We now focus on the metallicity distribution of the stars located in the overdense segment of eccentricity identified previously.

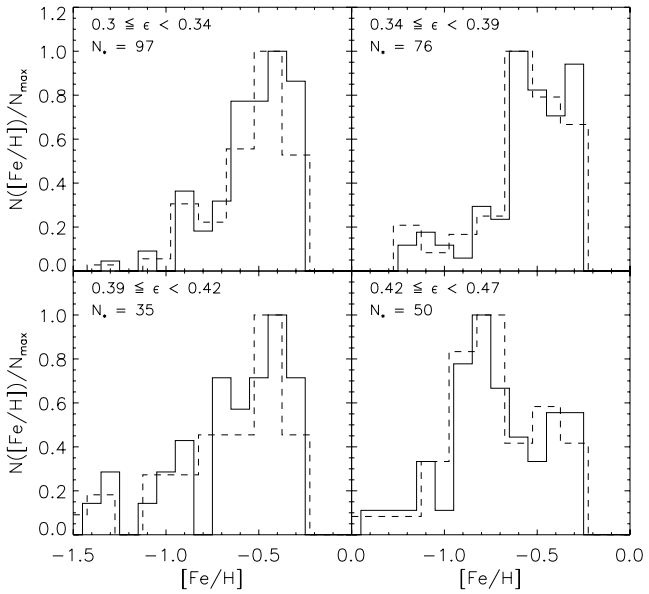

Figure 16. Distribution of metallicities for the stars located in the overdense segment of eccentricity identified in Section 4.3. Only those stars more metal-poor than [Fe/H] = −0.2 dex are shown. The different panels correspond to cuts in eccentricity, while the solid and dashed histograms are for metallicity bins of 0.1 and 0.15 dex, respectively. Note the distinctly different metallicity distribution of the stars with lowest (top left-hand panel) and the highest (bottom right-hand panel) eccentricities.

We have divided the eccentricity interval [0.3, 0.5) into four small intervals. The metallicity distribution obtained is shown in Fig. 16. The top panel corresponds to stars located near the lower limit, while the high-eccentricity end is shown in bottom right-hand panel. Note that the metallicity distribution of the stars in these two groups is very different. The stars with eccentricities close to $\epsilon \sim 0.3$ are predominantly more metal-rich, their distribution peaks around [Fe/H] ~ -0.4 dex. On the contrary, stars with high orbital eccentricity $\epsilon \sim 0.45$, are more metal-poor on average. Note as well, that there seems to be a third peak in metallicity [Fe/H] ~ -0.6 for stars with intermediate eccentricities, as depicted in the top right-hand panel.

It is clear that in all eccentricity ranges, there is a contribution from two or more groups of stars with similar metallicities. However, the relative contribution of these groups varies as the eccentricity changes. The fact that the characteristic metallicity of the stars in this region of the APL space varies with orbital eccentricity (in a discontinuous fashion) leads us to conclude that more than one disrupted galaxy has deposited debris in this region of phase space. Note that the single-satellite case would imply a narrow distribution of [Fe/H], which is independent of eccentricity, and is not consistent with Fig. 16.

Debris from disrupted galaxies is expected to have a somewhat extended distribution of eccentricities, as shown in Fig. 5. This fact together with the above analysis, suggests that it is better to identify the various satellites using the metallicity distribution of the stars in this region of phase space, rather than to do so on a purely dynamical basis.

We explore further this line of thought by separating the set of stars in this region of the APL space into three metallicity groups, according to the characteristics of the histograms shown in Fig. 16. We focus on three groups with [Fe/H] $\geqslant -0.45$ (Group 1; 120 stars), $-0.7 \leqslant$ [Fe/H] < -0.45 (Group 2; 86 stars) and $-1.5 \leqslant$ [Fe/H] < -0.7 (Group 3; 68 stars), which roughly correspond to the peaks/bumps seen in the right-hand panel of Fig. 14.

Fig. 17 shows the distribution of stars in this overdense region of the APL space, colour coded according to their metallicity. Note that there is considerable overlap between the different groups, but that some are more dominant in certain regions of phase space (as discussed before). For example, the more metal-rich stars preferentially have higher L_z for a given apocentre. Fig. 18 shows their velocity distribution. The 'banana' pattern in the upper panels is the same as that seen in Fig. 4 for satellite debris. Note that the more metal-rich stars (in blue; left-hand panels) tend to have significantly smaller z-velocities. In fact the z-velocity dispersion decreases with metallicity. For Group 1: $\sigma_z \sim 28\,\mathrm{km\,s^{-1}}$, for Group 2: $\sigma_z \sim 39\,\mathrm{km\,s^{-1}}$, while for Group 3: $\sigma_z \sim 52\,\mathrm{km\,s^{-1}}$. While a similar trend of increasing vertical velocity dispersion with metallicity exists for thin disc stars, it is by no means comparable to the abrupt changes seen for this set of stars. As a comparison, if we consider stars in the N04 sample with $\epsilon \leqslant 0.2$ and group them according to the same three metallicity bins, the z-velocity dispersions obtained are 16,

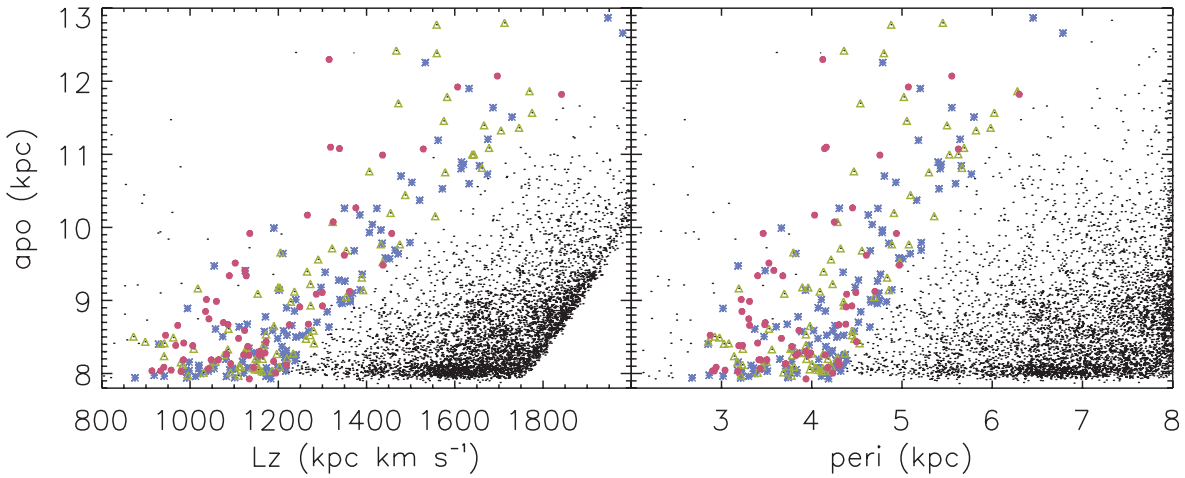

Figure 17. Identification of stars associated with the overdense region of constant eccentricity in the APL space. The (blue) asterisks correspond to Group 1 (120 stars), with [Fe/H] ∈ [−0.45, −0.2) dex; the (green) triangles to Group 2 (86 stars), with [Fe/H] ∈ [−0.7, −0.45) dex and the solid dots to Group 3 (68 stars), with [Fe/H] ∈ [−1.5, −0.7) dex. Note that the various groups are distributed slightly differently in the APL space. The black small dots correspond to all stars in the N04 sample with [Fe/H] < −0.2 dex.

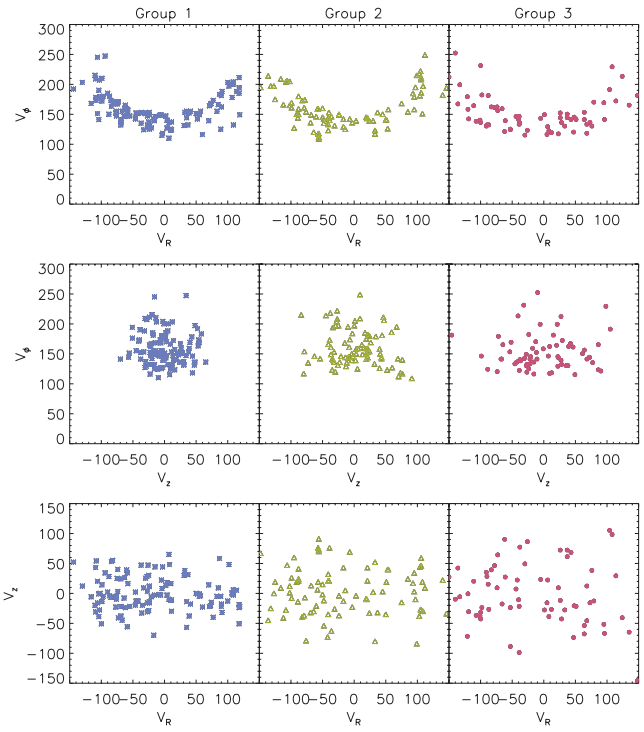

Figure 18. Velocities of stars (in km s^{-1}) associated with the groups shown in Fig. 17. Note that the velocity distribution in the z-direction (second and third panels) is very different for each group. Compare to the velocity distribution of satellite debris shown in Fig. 4.

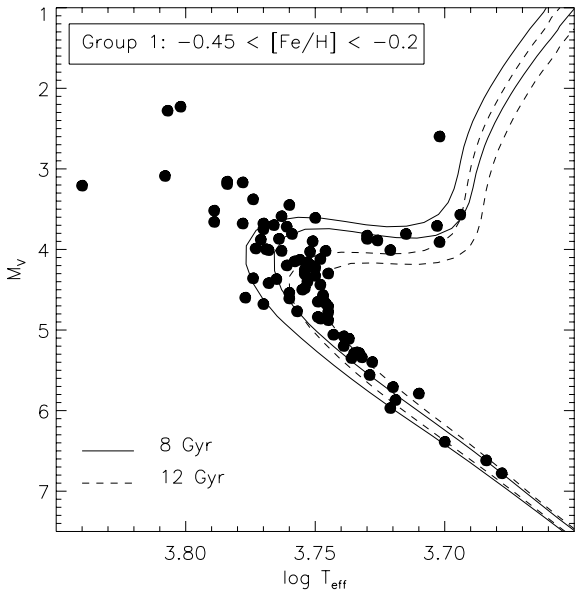

Figure 19. HR diagram for the 88 single stars in Group 1. The uncertainty in the location of a star in this diagram is $\sim$ 50–100 K in the x-direction and 0.2 mag in the y-direction, that is roughly twice the symbol size. Overplotted are two sets of isochrones with metallicities close to the maximum (right-most) and minimum values (left-most) found in this group, and for an 8-Gyr-old population (solid) and a 12-Gyr-old population (dashed). In all cases, the isochrones correspond to an α-enhanced population, with [α/Fe] = 0.4 dex.

19 and 19.5 km s^{-1}, respectively, i.e. almost independent of [Fe/H]. For higher eccentricity stars, those with $0.2 \leqslant \epsilon \leqslant 0.3$, σ_z is 23, 30 and 32 km s^{-1} in the same three metallicity bins, again indicative of small variations with [Fe/H]. Therefore, the strong dependence of the z-velocity dispersion with metallicity found for the stars in the overdense segment of constant eccentricity of the APL space is unique to this special set of stars. It constitutes another manifestation of the particular nature of the stars found in this region of phase space.

4.5.2 Age distribution

Let us now focus on the age distribution of the stars in Groups 1–3. The most reliable way to determine the age pattern of these stars is by means of their HR diagram. We prefer not to use the individual ages derived by N04 because of the large error bars. The determination of individual ages for stars is subject to large uncertainties, and it is more reliable to try to establish whether the stars in a given group are mostly young or old, and to obtain a rough estimate of their ages using isochrones. Since binary stars generally introduce more scatter in the HR diagram, we will not include these in the analysis. The identification of binaries has been done spectroscopically and visually (see Section 3.2.4 of N04).

The uncertainty in the location of a star in the HR diagram comes from two sources. Since the average error in the temperature is small (of the order of 50-100 K), it is mostly driven by uncertainties in the absolute magnitude, which arise from the distance determination. On average, the relative distance errors are in the 10–13 per cent range. This implies an uncertainty in the absolute magnitude of $\sim$0.2 mag.

In Fig. 19 we plot the HR diagram of the 88 single stars in Group 1. It shows some very distinct features: (i) there are very few young stars; (ii) there is evidence of two turn-off points around $M_V \sim 3.7$ and $M_V \sim 4$; (iii) there is a clearly demarcated subgiant branch region. To establish whether and how these features are linked, we have explored the Yonsei–Yale single stellar population library[5] by Yi et al. (2001), and last updated by Demarque et al. (2004). In Fig. 19, we overplot the sets of isochrones that best match the various features as judged by eye-ball inspection. Two isochrones correspond to a low age of 8 Gyr (solid curves), which fit well the location of the brightest turn off (TO) point. Each of these two isochrones is for a different metallicity that is close to the maximum and minimum values found in Group 1: -0.5 and -0.25 dex, respectively. A second set of (older) 12-Gyr isochrones (dashed curves) reproduces well the location of the fainter TO point, and yields an almost perfect match to the location of the stars on the upper main sequence.

We can obtain an estimate of the relative importance of the two populations by focusing on the region delimited by $3.5 \leqslant M_V \leqslant 5.5$, where the 8- and 12-Gyr isochrones show the least overlap. We shall say that a star belongs to the 8-Gyr (12-Gyr) population if it is found to the left-hand side (right-hand side) of the most metal-rich 8-Gyr isochrone. Out of the 73 stars located in this region, 25 can be associated with the younger isochrone, while the remaining 48 appear to be older. Therefore, the ratio of the young to the old population in Group 1 is roughly 1:3 versus 2:3 with respect to the total number of stars in this group. It is worth noting that the kinematics of these two populations are indistinguishable from one another.

Fig. 20 shows the HR diagram for the 57 single stars in Group 2. Like in the case of Group 1, few young stars are present, and the subgiant and the bottom of the red giant branches can be

[5] http://www-astro.physics.ox.ac.uk/~yi/yyiso.html

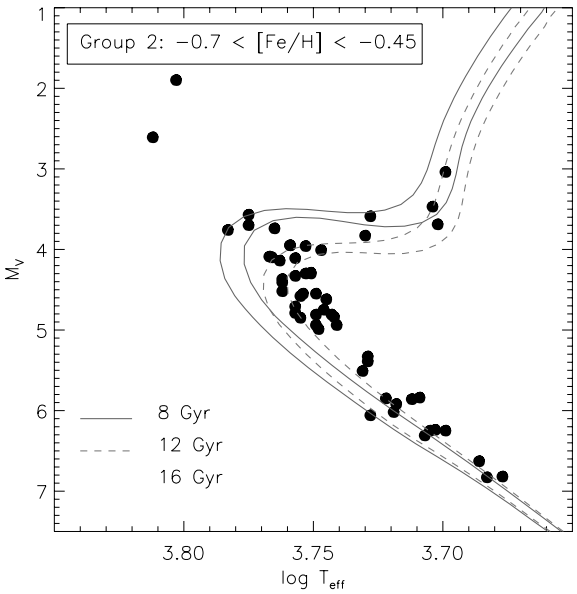

Figure 20. HR diagram for the single stars in Group 2. Overplotted are three sets of isochrones with metallicities close to the maximum (right-most) and minimum values (left-most) found in the group, and for $[\alpha/\mathrm{Fe}] = 0.4$ dex. The 8 Gyr (solid) reproduces well the location of the TO point around $M_V \sim 3.6$. The intermediate 12-Gyr isochrone (dashed) matches the second TO point at $M_V \sim 4.5$, while an older 16-Gyr isochrone appears to be required to fit the location of the stars around $M_V \sim 4.7$ and $\log T_{\rm eff} \sim 3.74$. Compare with the HR diagrams of Groups 1 and 3 shown in Figs 19 and 21, respectively.

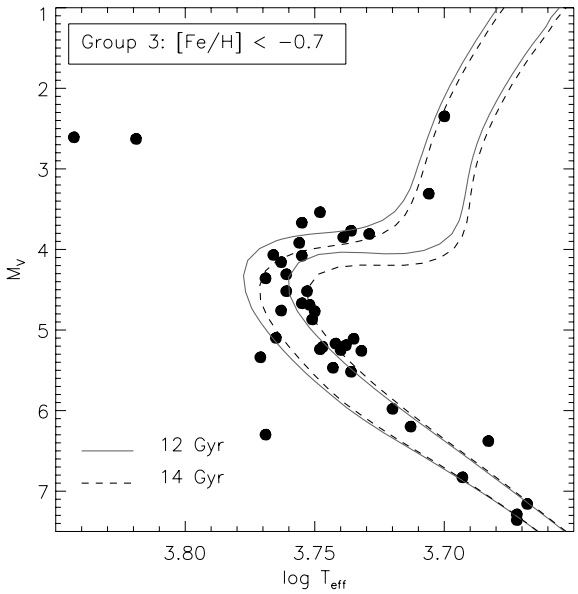

Figure 21. HR diagram of all single 41 stars in Group 3. Overplotted are two sets of isochrones with similar metallicity as the maximum (right-most) and minimum values ($[\mathrm{Fe/H}] \sim -1$ dex; left-most) and to 12 Gyr (solid) and 14 Gyr (dashed) of age, for $[\alpha/\mathrm{Fe}] = 0.4$ dex. Unlike for Groups 1 and 2, the stars in Group 3 are consistent with having all the same age, around 14 Gyr.

clearly identified. Furthermore, besides the two TO points visible around $M_V \sim 3.6$ and $M_V \sim 4$, there is possibly a third turn-off point at $M_V \sim 4.5$. We have overplotted the 8- and 12-Gyr-old isochrones for two metallicities $[\mathrm{Fe/H}] = -0.75$ dex and $[\mathrm{Fe/H}] = -0.5$ dex, which are close to the maximum and minimum values found in this group. Note that none of the 8- and 12-Gyr-old isochrones provides a good match to the group of stars with $M_V \sim 4.7$ and $\log T_{\rm eff} \sim 3.74$. This is why we have also plotted a third set of isochrones corresponding to an age of 16 Gyr which fit the features better. We estimate the relative importance of the populations associated with these three sets of isochrones by focusing on the region in the HR diagram defined by $3.5 \leqslant M_V \leqslant 5.5$. Out of the 41 single stars located here, six can be associated with the 8-Gyr-old isochrones (∼15 per cent), 15 stars (∼36 per cent) to the 12-Gyr-old isochrones and the remaining 20 stars (∼49 per cent) to the 16-Gyr-old isochrones.

In Fig. 21 we show the HR diagram of Group 3. In this case, the dearth of young stars is even more striking than for Groups 1 and 2. Like before, the subgiant and red giant branches are quite prominent. However, only one TO point can be clearly identified for Group 3, around $M_V \sim 4.3$. This TO is fainter than what was found for Group 1 and is slightly brighter than the weakest one in Group 2. For completeness, we have overplotted two sets of isochrones for 12 and 14 Gyr, but the overall features of the HR diagram seem to be well reproduced by the older 14-Gyr isochrone.

In our exploration of the stellar population libraries, we have found that better matches to the location of the features (especially the main sequence) in the various HR diagrams could be obtained for α-enhanced populations, in particular those with $[\alpha/\mathrm{Fe}] = 0.4$. This α-enhancement is of similar magnitude to that found in Galactic halo stars, although it occurs at a relatively high-metallicity ($[\mathrm{Fe/H}] \geqslant -1$ dex) compared to the halo. This result would suggest that the stars in Groups 1–3 were formed from material that had been previously enriched both by type I and type II supernovae, but predominantly by the latter. Undoubtedly spectroscopic abundances are required to confirm this speculation.

We now summarize the discoveries made in the last two sections. Recall that the dynamical analysis of the APL space suggested the presence of an excess of stars located in a segment of constant eccentricity, with $0.3 \leqslant \epsilon < 0.5$. In Section 4.4, we separated these stars into Groups 1–3 on the basis that the metallicity distribution was varying with eccentricity in a discontinuous fashion within this segment (Fig. 16). We then found that these three groups of stars also have slightly different kinematics, particularly in the vertical (z) direction (Fig. 18). Finally, we showed that the age distribution of the stars varies from group to group, a point that is clearly visible from simple inspection of the respective HR diagrams (Figs 19–21). Using single stellar population models, we quantified these differences, and found evidence that Group 1 is formed by two populations of 8 and 12 Gyr of age (33 and 66 per cent, respectively); Group 2 by three populations of 8 Gyr (only 15 per cent), 12 Gyr (36 per cent) and 16 Gyr (49 per cent) and Group 3 is consistent with just one 14-Gyr-old population. Therefore, the three groups we identified are distinct in metallicity, kinematics as well as in their age distribution.

5 SUMMARY AND CONCLUSIONS

We have analysed the Geneva–Copenhagen survey of nearby, predominantly disc, stars. This is the largest compilation of stars with accurate and complete spatial and kinematic information, and for which metallicities (derived from Strömgren photometry) are available (99 per cent of the sample). We started this project with the goal of quantifying the amount of substructure associated to mergers that the Milky Way galaxy experienced in its evolution.

To guide the search for the remains of past minor mergers, we analysed numerical simulations of the disruption of satellite

galaxies. We focused first on the time-independent regime (satellite plus static host galaxy), and secondly on the cosmological simulations of the formation of disc galaxies by Abadi et al. (2003a). In both cases, we found that substructure is present in the space defined by apocentre, pericentre and z-angular momentum: the APL space. While both apocentre and pericentre depend on the functional form of the galaxy's gravitational potential, perfect knowledge is not required for the substructure to become apparent. Furthermore, such correlations are not significantly altered by orbital evolution due to changes in the mass distribution or to dynamical friction. It is true, however, that stars released in different perigalactic passages have slightly different orbital properties, and hence will generally be located in several smaller lumps in the APL space. However, these lumps are located along a segment of constant eccentricity, thereby permitting the assessment of a common origin. Furthermore, we found that the substructure present in the APL space remains coherent for many Gyrs, well after the merger has fully mixed.

The APL space for the N04 catalogue shows large amounts of substructure. The most prominent structures are related to the superclusters Hyades–Pleiades, Sirius and Hercules; and are most likely due to dynamical perturbations induced by the spiral arms and the Galactic bar (Famaey et al. 2005). These structures are composed of stars on disc-like orbits with relatively low eccentricity. The age distributions of the HyPl and the Sirius superclusters are indistinguishable from that of the full N04 sample, while Hercules appears to have a more prominent old population. On the other hand, the metallicity distributions of the stars in these superclusters are very similar and typical for the thin disc, peaking at $[\mathrm{Fe/H}] \sim -0.13$ dex for Hercules, -0.08 dex for HyPl and -0.18 dex for Sirius with a dispersion of $\sim$0.2 dex in all cases.

The detailed statistical analysis of the APL space reveals the presence of around 10 other overdensities at significance levels higher than 99 per cent. Unlike the case of the superclusters, these overdensities are located along two to three segments of constant eccentricity, as predicted for substructures that are the result of minor mergers. There are 274 stars in this region of the APL space, which is delimited by eccentricity $0.3 \leqslant \epsilon < 0.5$. The metallicity distribution of these stars is inconsistent with that of the whole N04 sample at the 10^{-8} level, as quantified by a KS test. Furthermore, the HR diagram shows unambiguously that these stars are predominantly old; prominent subgiant and red giant branches are easily distinguishable, and the very few young stars present are put in evidence by a turn-off point around $M_V \sim 3.8$–4. All this strongly supports the hypothesis that these substructures represent the remains of satellite galaxies that merged with the Milky Way several Gyrs ago.

The metallicity distribution of the stars in this overdense region of the APL space varies with eccentricity in a discontinuous fashion. This allows the separation of these stars into three Groups, which we believe represent at least three accreted galaxies. These three groups of stars are dissimilar not only in their metallicity distribution, but also have different kinematics in the vertical (z) direction and distinct age distributions. The most metal-rich group ($[\mathrm{Fe/H}] > -0.45$ dex) has 120 stars which are distributed into two stellar populations of 8 Gyr (33 per cent) and 12 Gyr (67 per cent) of age, as deduced by comparison to the isochrones by Yi et al. (2001) and from the presence of two turn-off points at $M_V \sim 3.7$ and $M_V \sim 4$. The second Group with $\langle[\mathrm{Fe/H}]\rangle \sim -0.6$ dex has 86 stars, and is constituted by three populations of 8 Gyr (15 per cent), 12 Gyr (36 per cent) and 16 Gyr (49 per cent). Finally, the third Group has 68 stars, with typical metallicity around -0.8 dex, and which appear to be part of a single 14-Gyr-old population. Whereas none of the Groups was identified as such previously, there seems to be considerable overlap between Group 2 and the Arcturus 'stream' (Navarro et al. 2004), both in their kinematics as in their metallicities.

The characterization of the progenitor galaxies, either in terms of their initial mass or their stellar properties is possible in this case thanks to the multifaceted nature of the N04 sample. A direct comparison to the numerical simulation presented in Section 3.2 suggests that the accreted satellites had an initial mass $\sim 4 \times 10^8\,\mathrm{M}_\odot$ (much lower masses can be excluded on the basis of their extent in the APL space). The relatively high-metallicity characteristic of these groups is consistent with the expected correlation between luminosity (or mass) and [Fe/H] found in present-day galaxies (Mateo 1998). Further insight into the properties of these building blocks could be gained from high-resolution spectroscopy. Knowledge of the detailed abundance patterns could prove to be extremely useful as a way of confirming the origin and the history of the different groups (Freeman & Bland-Hawthorn 2002).

The substructures identified cannot be uniquely associated to a single traditional Galactic component, since they are in a transition region that overlaps with both the thin and the thick discs. This assessment is based on the metallicity distribution of their stars (peak values in the range -0.4 to -0.8 dex) as well as on their vertical velocities ($\sigma_z \sim 28$–$52\,\mathrm{km\,s^{-1}}$). The identification of debris in the Galactic discs whose origin can be traced back to more than one satellite galaxy provides support to the accretion scenario for the formation of the thick disc (Abadi et al. 2003b). However, it is not clear how this scenario differs from the dynamical heating of a previously existing thin disc by (in this case, more than) one minor merger. In this context, a natural next step consists in establishing how the properties of a pre-existent thin disc differ dynamically from those of accreted satellites (Villalobos & Helmi, in preparation).

Our findings suggest that the peak in the merging activity that led to the Milky Way has taken place before $z \sim 1$ for a ΛCDM cosmology, with little accretion of (relatively) massive galaxies after that. This is not unlike the results of the simulations of Abadi et al. (2003b).

An important issue raised by this study concerns the traditional separation of the Galaxy into distinct components, and its description in terms of a set of coarse-grained distribution functions that satisfy Jeans theorems (Binney & Tremaine 1987). The Galactic disc appears not to be in steady state, i.e. its phase-space density is probably changing in time as a result of the perturbations produced by spiral density waves and the Galactic bar. Moreover, we found that the fine-grained distribution function still contains substantial discernible information about the evolutionary history of the Galaxy. It will be essential to establish how to optimally characterize the phase-space structure of the Galaxy taking into account its graininess, particularly in the context of billion-star surveys such as Gaia (Binney 2005).

Galactic structure has come to be a very complex field. The vast data sets that will become available in the near future, such as RAVE (Steinmetz 2003), SDSS-II with SEGUE and ultimately Gaia (Perryman et al. 2001) will drive this to a summit. However, access to such complexity and richness is the key to disentangle the dynamical and evolutionary history of the Milky Way. Through studies like that presented here, we should hope to eventually be able to reconstruct the star formation, chemical enrichment pattern and evolutionary history of the building blocks of galaxies.

ACKNOWLEDGMENTS

Eline Tolstoy is gratefully acknowledged for very stimulating discussions. The anonymous referee is thanked for constructive

comments. We have made use of the Besancon model of the Galaxy and are very grateful to Annie Robin and her collaborators for making such a useful tool accessible to the community. This work has been partially financed by the Netherlands Organization for Scientific Research (NWO). JFN acknowledges support from the Alexander von Humboldt Foundation and from the Leverhulme Foundation. BN gratefully acknowledges substantial financial support from the Carlsberg Foundation, the Danish Natural Science Research Council, the Swedish Research Council, the Nordic Academy for Advanced Study and the Royal Physiographic Society in Lund.

REFERENCES

Abadi M. G., Navarro J. F., Steinmetz M., Eke V. R., 2003a, ApJ, 591, 499
Abadi M. G., Navarro J. F., Steinmetz M., Eke V. R., 2003b, ApJ, 597, 21
Alonso A., Arribas S., Martínez-Roger C., 1996, A&A, 313, 873
Bekki K., Chiba M., 2001, ApJ, 558, 666
Benson A. J., Bower R. G., Frenk C. S., Lacey C. G., Baugh C. M., Cole S., 2003, ApJ, 599, 38
Binney J., 2005, in Turon C., O'Flaherty K. S., Perryman M., eds, ESA SP-576, Proc. Three Dimensional Universe with Gaia. ESA Publications, Noordwijk, p. 87
Binney J., Tremaine S., 1987, Galactic Dynamics. Princeton Univ. Press, Princeton, NJ
Brook C. B., Kawata D., Gibson B. K., Freeman K. C., 2004, ApJ, 612, 894
Carney B. W., Latham D. W., Laird J. B., 1990, AJ, 99, 572
Cayrel R. et al., 2004, A&A, 416, 1117
Chereul E., Crézé M., Bienaymé O., 1998, A&A, 340, 384
Chiba M., Beers T. C., 2001, ApJ, 549, 325
Crawford D. L., 1975, AJ, 80, 955
Dehnen W., 1998, AJ, 115, 2384
Dehnen W., 2000, AJ, 119, 800
Dehnen W., Binney J. J., 1998, MNRAS, 298, 387
Demarque P., Woo J. H., Kim Y. C., Yi S., 2004, ApJS, 155, 667
De Simone R., Wu X., Tremaine S., 2004, MNRAS, 350, 627
Edvardsson B., Andersen J., Gustafsson B., Lambert D. L., Nissen P. E., Tomkin J., 1993, A&A, 275, 101
Eggen O. J., 1958, MNRAS, 118, 65
Eggen O. J., 1960, MNRAS, 120, 563
Eggen O. J., 1975, PASP, 87, 37
Eggen O. J., 1996, AJ, 112, 1595
Eggen O. J., Lynden-Bell D., Sandage A. R., 1962, ApJ, 136, 748
ESA 1997, The Hipparcos and Tycho Catalogues, ESA-SP 1200
Famaey B., Jorissen A., Luri X., Mayor M., Udry S., Dejonghe H., Turon C., 2005, A&A, 430, 165
Flynn C., Sommer-Larsen J., Christensen P. R., 1996, MNRAS, 281, 1027
Freeman K. C., Bland-Hawthorn J., 2002, ARA&A, 40, 487
Fux R., 2001, A&A, 373, 511
Gould A., 2003, ApJ, 592, L63
Governato F. et al., 2004, ApJ, 607, 688
Helmi A., White S. D. M., 1999, MNRAS, 307, 495
Helmi A., de Zeeuw P. T., 2000, MNRAS, 319, 657
Helmi A., White S. D. M., de Zeeuw P. T., Zhao H., 1999, Nat, 402, 53
Helmi A., White S. D. M., Springel V., 2003, MNRAS, 339, 834
Høg E. et al., 2000, A&A, 355, L27
Ibata R. A., Gilmore G., Irwin, M. J., 1994, Nat, 370, 194
Johnston K. V., 1998, ApJ, 495, 297
Johnston K. V., Hernquist L., Bolte M., 1996, ApJ, 465, 278
Jørgensen B. R., Lindegren L., 2005, A&A, 436, 127
Knebe A., Gill S., Kawata D., Gibson B. K., 2005, MNRAS, 357, 35
Martin N. F., Ibata R. A., Bellazzini M., Irwin M. J., Lewis G. F., Dehnen W., 2004, MNRAS, 348, 12
Mateo M., 1998, ARA&A, 36, 435
Mayer L., Moore B., Quinn T., Governato F., Stadel J., 2002, MNRAS, 336, 119
Mo H. J., Mao S., White S. D. M., 1998, MNRAS, 295, 319
Momany Y., Zaggia S. R., Bonifacio P., Piotto G., De Angeli F., Bedin L. R., Carraro G., 2004, A&A, 421, L29
Navarro J. F., Helmi A., Freeman K. C., 2004, ApJ, 601, L43
Nissen P. E., Schuster W. J., 1991, A&A, 251, 457
Nordström B. et al., 2004, A&A, 418, 989 (N04)
Norris J. E., Ryan S. G., 1989, ApJ, 340, 739
Olsen E. H., 1983, A&AS, 54, 55
Olsen E. H., 1984, A&AS, 57, 443
Olsen E. H., 1993, A&AS, 102, 89
Olsen E. H., 1994a, A&AS, 104, 429
Olsen E. H., 1994b, A&AS, 106, 257
Perryman M. A. C. et al., 1998, A&A, 331, 81
Perryman M. A. C. et al., 2001, A&A, 369, 339
Press W. H., Flannery B. P., Teukolsky S. A., Vetterling W. T., 1988, Numerical Recipies in FORTRAN: The Art of Scientific Computing. Cambridge Univ. Press, Cambridge
Quillen A. C., Minchev I., 2005, AJ, 130, 576
Raboud D., Grenon M., Martinet L., Fux R., Udry S., 1998, A&A, 335, L61
Robertson B., Bullock J. S., Font A. S., Johnston K. V., Hernquist L., 2005, ApJ, 632, 872
Robin A. C., Reylé C., Derrière S., Picaud S., 2003, A&A, 409, 523
Robin A. C., Reylé C., Derrière S., Picaud S., 2004, A&A, 416, 157
Samland M., Gerhard O., 2003, A&A, 399, 261
Sandage A., Fouts G., 1987, AJ, 93, 74
Schuster W. J., Nissen P. E., 1989, A&A, 221, 65
Silk J., Bouwens R., 2001, New Astron. Rev., 45, 337
Sommer-Larsen J., Götz M., Portinari L., 2003, ApJ, 596, 47
Spergel D. N. et al., 2003, ApJS, 148, 175
Springel V., Hernquist L., 2003, MNRAS, 339, 289
Steinmetz M., 2003, in Munari U., ed., ASP. Conf. Ser. Vol. 298, Gaia Spectroscopy, Science and Technology. Astron. Soc. Pac., San Francisco, p. 381
Unavane M., Wyse R. F. G., Gilmore G., 1996, MNRAS, 278, 727
Venn K. A., Irwin M., Shetrone M. D., Tout C. A., Hill V., Tolstoy E., 2004, AJ, 128, 1177
Yanny B. et al., 2003, ApJ, 588, 824
Yi S., Demarque P., Kim Y. C., Lee Y. W., Ree C. H., Lejeune T., Barnes S., 2001, ApJS, 136, 417
Zaritsky D., White S. D. M., 1988, MNRAS, 235, 289

This paper has been typeset from a TEX/LATEX file prepared by the author.